UNIVERSITY OF CALIFORNIA SAN DIEGO

Subtidal and Tidal Circulation on a Rocky Shoreline

A thesis submitted in partial satisfaction of the
requirements for the degree Master of Science

in

Oceanography

by

Kaden James Quinn

Committee in charge:

Professor Falk Feddersen, Chair
Professor Janet Becker
Professor Mark Merrifield

2024

The Thesis of Kaden James Quinn is approved, and it is acceptable in quality and form for publication on microfilm and electronically.

University of California San Diego

2024

TABLE OF CONTENTS

LIST OF FIGURES

LIST OF TABLES

ACKNOWLEDGEMENTS

I would first like to acknowledge Professor Falk Feddersen for serving as my committee chair and for being a fantastic mentor during my time at Scripps Institute of Oceanography. Next, professor Mark Merrifield and professor Janet Becker for serving on my committee and for there valuable feedback. Olavo Marques, James MacMahan, and Ata Suanda for there guidance throughout the analysis process. My lab mates Kanoa Pick and Drew Davey for serving as constant inspirations. Everyone who helped deploy and recover the instruments during the ROXSI experiment. The amazing community at Scripps Institute of Oceanography from my professors, to academic advisors, and fellow students. Finally, I would like to acknowledge to my family and friends for always supporting me.

ABSTRACT OF THE THESIS

Subtidal and Tidal Circulation on a Rocky Shoreline

by

Kaden James Quinn

Master of Science in Oceanography

University of California San Diego, 2024

Professor Falk Feddersen, Chair

Coastal circulation studies have focused largely on alongshore uniform sandy coastlines and some coral reef regions. Circulation on rocky shorelines has received much less attention. Rocky shorelines have significantly more bathymetric variability across a range of scales. Here we analyze the inner-shelf depth-averaged circulation at China Rock on the Monterey Peninsula CA with an array of 15 ADCPs deployed for a six week duration between 24 m and 3 m mean water depth, spanning 800 m in the cross-shore and 600 m in the alongshore with concurrent surface gravity wave and wind stress observations.

The depth-averaged circulation is dominated by the subtidal, diurnal, and semidiurnal frequency bands with no preferred sense of circulation rotation. Counter to that on a sandy inner-

shelf, the principal-axes ellipses decay onshore indicating the effect of strong bottom friction and there is variability in the axis orientations indicating steering by the larger-scale bathymetric variations. Analysis is focused on three regions: the offshore, midshore, and near-bay regions. In the offshore and midshore regions, a subtidal balance between alongshore wind stress and linear bottom friction has skill consistent with previous studies.

Estimates of the linear drag coefficient in 8-24 m water depth are much larger than on sandy inner-shelves which is due to the large bathymetric roughness present at China Rock. In the embayment but not in regions of wave breaking, the cross-shore subtidal flow is linearly related to the onshore Stokes-drift transport, indicating it is wave driven. However, the return flow is stronger than expected for an open coast inner-shelf. The ratio of return flow magnitude to Stokes-drift transport is consistent with the variations in the embayment geometry. In the tidal bands, the cross-shore velocity decay indicates the strong effect of bottom stress, far larger than those observed across the sandy continental shelf of North Carolina or on a fringing coral reef shelf on the western coast of O'ahu, Hawai'i. The depth-averaged circulation along rocky shorelines is analogous to sandy shorelines but with much elevated bottom stress effect.

Chapter 1

Introduction

The inner shelf is an important transition region defined between the surf zone where depth-limited wave breaking occurs and the mid shelf where the surface and bottom boundary layers no longer overlap (Weisberg et al., 2001; Austin and Lentz, 2002; Lentz and Fewings, 2012). Circulation in this region controls the flow of plankton, pollutants, and particles that directly affect the health of ecosystems (e.g., Morgan et al., 2018; Moulton et al., 2023) as well as the cross-shore exchange of heat (e.g., Fewings and Lentz, 2011; Sinnett and Feddersen, 2019). Inner shelf circulation studies have mostly been restricted to sandy coastlines (Lentz and Fewings, 2012), with additional coral reef studies (e.g., Monismith, 2007; Hench et al., 2008; Arzeno et al., 2018). Rocky shorelines comprise between 33-75% of the total global coastline (Johnson, 1988.; Bird, 2008; Luijendijk et al., 2018). Despite their prevalence, studies of the circulation on rocky shorelines are limited.

Inner shelf circulation studies have often focused on depth-averaged currents (Lentz et al., 1999). On subtidal ($>$ 33 h in mid-latitudes) time scales, alongshore circulation is largely driven by along shelf winds, and the resulting momentum balance is dominated by the wind stress, pressure gradient, and bottom stress (e.g., Mitchum and Clarke, 1986; Lentz and Winant, 1986; Lentz, 1994; Lentz et al., 1999; Fewings and Lentz, 2010; Kumar et al., 2015). On shorter tidal ($\approx$ 12 and $\approx$ 24 h) time scales, alongshore circulation on the inner-shelf is driven by barotropic tides, and the momentum balance is largely between local rate of change, bottom stress and

pressure gradient (Lentz et al., 2001; Arzeno et al., 2018; Amador et al., 2020). The dynamical balances in subtidal and tidal band on a rocky inner-shelf has received less attention. Across time scales, the bottom stress is a key component of the inner-shelf alongshore momentum balance (Trowbridge and Lentz, 2018). A variety of bottom stress parameterizations have been used typically involving a linear drag law for subtidal studies (e.g., Lentz et al., 1999) or quadratic drag laws in the tidal band (e.g., Arzeno et al., 2018). It unknown how well these bottom stress parameterizations work on rocky inner-shelves or how their drag coefficient varies or compares to sandy or coral reef inner-shelves.

In the cross-shore, Stokes drift by surface gravity waves has been shown to drive offshore depth-averaged flow (Lentz et al., 2008). The strength of the observed cross-shore flow has been found to differ from expected cross-shore flow and this difference has been attributed to bathymetric variability (Kirincich et al., 2009). Embayment geometry and the incident wave conditions have been shown to strongly affect cross-shore circulation for sandy bays with alongshore widths W of $O(100\text{ m})$ (Castelle and Coco, 2013) and rocky surge channels $W = O(1\text{-}10\text{ m})$ (MacMahan et al., 2023). Surface circulation has recently been studied for a rocky embayment $W = 200$ m and was found to be dominated by a rip current (Conlin et al., 2024). However, the depth-averaged circulation near a rocky embayment in conjunction with the circulation on a rocky inner shelf has yet to be studied.

Rocky shorelines have significantly more bathymetric variability at a variety of spatial scales when compared to other types of shorelines such as coral reefs and sandy beaches. On length-scales of (4-64 m), rocky shorelines vertical variability is three times larger than a Western O'ahu coral reef (MacMahan et al., 2024). This is likely due to features such as bedrock walls, sloping ledges, offshore banks and pinnacles MacMahan et al. (2023). On larger $O(100\text{ m})$ length-scales, rocky shorelines tend to feature embayments that can span large scales in the alongshore and cross-shore (Limber et al., 2014; Limber and Murray, 2014). It is unknown how this large variability at such a wide variety of scales will affect circulation overall on rocky shorelines.

Here we investigate the subtidal and tidal circulation on the inner-shelf off a rocky shoreline on the Monterey peninsula (CA, USA) with month-long observations of currents, wind, waves, and tide. This paper is organized as follows. In section 2, observations of the study site and analysis methods are described. In section 3.1, the depth-averaged circulation is examined across frequency bands using spectral and principal component analysis. In sections 3.2 the circulation due to wind-stress and surface gravity waves are examined on subtidal time scales, while in section 3.3, the circulation due to the barotropic tide is examined on tidal time scales. In sections 4.1, subtidal circulation between a rocky and sandy shoreline are compared. In 4.2, estimates of linear drag are compared with physical bottom roughness. In 4.3, wave driven circulation is examined in the context of the near-bay. In Section 4.4, tidal phase shifts and attenuation of currents on a rocky shoreline are compared with a sandy shoreline and coral reef. Results and discussion are summarized in section 5.

Chapter 2

Observations and Methods

The first ROXSI (ROcky shores: eXperiments and SImulations) experiment occurred at China Rock, Pebble Beach, CA during summer of 2022 from June 24th to July 20th. China Rock was chosen as a study site due to the wide range of scales of rocks that cover the shoreline from the intertidal zone to far offshore. Unlike sandy shorelines, rocky shorelines only change on geological time scales and thus the bathymetry remained constant for the duration of the experiment.

Bathymetric data at China Rock was sourced from National Oceanic and Atmospheric Administration (NOAA), California State University, Monterey Bay (CSUMB), a survey performed by the Joint Airborne Lidar Bathymetry Technical Center of Expertise (JALBTCX) and a DiveJet survey performed by Naval Postgraduate School (Marques 2023 et al.). A China Rock coordinate system is then defined such that x is in the cross shore (with $-x$ is directed towards 285°N) and y is in the along shore. In the cross-shore, large scale variability at China Rock can be described by its moderate (1:40) cross-shore slope. In the alongshore, large scale variability is defined by the bay at $(x,y) = (0,0)$ m bounded by two headlands to the north and south. The apex of the northern headland is located at $y = 125$ and extends approximately to $x = -100$. The apex of the southern headland is at $y = -200$ and extends slightly further offshore to $x = -150$. On smaller bathymetric scales, the wide range of rocks leads to very high bottom roughness. This bottom roughness can be quantified by examining 5×5 m squares of the 2 m gridded

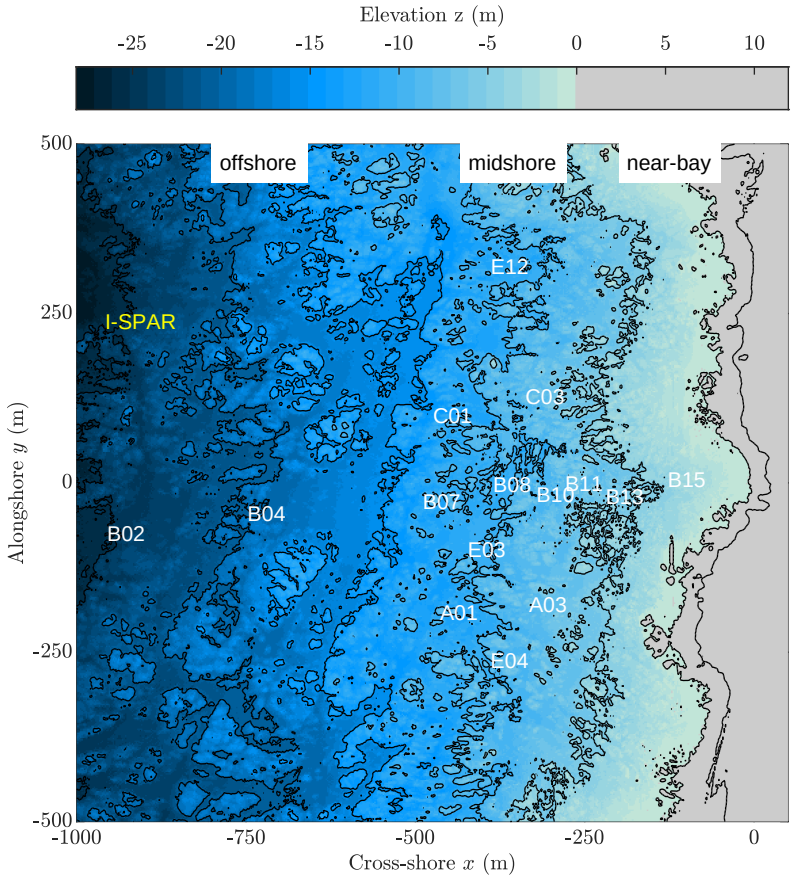

Figure 2.1. Elevation z relative to mean sea level gridded to 2 m horizontal resolution as a function of cross-shore x and alongshore y China Rock coordinate system. Contour lines are at 5 m intervals. White text is the ID of each Acoustic Doppler current profiler (ADCP). Yellow text shows the mean location of the I-SPAR. General span of the offshore, midshore and near-bay regions indicated by labels.

bathymetry data at China Rock. The standard deviation within these squares had a median of 0.5 m while the range between the maximum and minimum in value in each square across the study sight had a median of 2 m (Marques 2023).

The subsurface array of instruments consisted of 15 Acoustic Doppler Current Profilers (ADCPs- see figure 2.1), a combination of Nortek Signature 1000s and Aquadopps, that provide measurements of waves and currents. The ADCPs were arranged in three cross-shore lines and one alongshore line. The B line is the longest cross-shore line and spans from the edge of the

Table 2.1. List of ADCP IDs, instrument types, sampling schemes, mean depth during the experiment, height of the transducer above the bottom (HAB) and bin size. Signature1000 sampling schemes are continuous. Aquadopp sampling schemes are split between profile interval/average interval.

ID	Instrument	Sampling Scheme	Mean depth (m)	Bin size Δz (m)
A01	Signature1000	8 Hz	12.7	0.5
A03	Aquadopp 2 MHz	30/30 s	8.4	0.5
B02	Aquadopp 600 kHz	600/300 s	24.5	2.0
B04	Aquadopp 1 MHz	30/1 s	20.1	1.0
B07	Aquadopp 1 MHz	30/1 s	13.4	1.0
B08	Aquadopp 1 MHz	1/1 s	10.7	1.0
B10	Signature1000	8 Hz	9.6	0.5
B11	Aquadopp 2 MHz	1/1 s	8.9	0.5
B13	Signature1000	4 Hz	4.8	0.5
B15	Signature1000	4 Hz	3.1	0.5
C01	Signature1000	8 Hz	13.2	0.5
C03	Aquadopp 1 MHz	30/30 s	8.5	0.5
E03	Aquadopp 1 MHz	1/1 s	9.0	1.0
E04	Aquadopp 1 MHz	1/1 s	10.1	1.0
E12	Aquadopp 1 MHz	1/1 s	11.4	1.0

array offshore to the bay onshore. The shorter cross-shore lines are the A and C lines which extend off the headlands. The E line stretches alongshore through the center of the array from just north and south of the headlands.

The ADCPs were deployed in varying water depths (table 2.1) with a mix of vertical resolutions and sampling schemes. Here, the analysis is focused on the circulation on subtidal and tidal time scales. Thus current observations are depth and hourly averaged. Vertical averaging is performed using all ADCP bins except those that are closer than 1 bin size from the mean surface. Current components are rotated into the China Rock coordinate system with a cross-shore u and alongshore v current. Hourly wave statistics and sea surface elevation are computed from ADCPs integrated pressure sensor. Significant wave height H_s, mean period T_a, and mean direction θ are computed for the sea-swell band of frequencies from 0.06 Hz $\leq f \leq$ 0.20 Hz at each location. Wave direction is rotated into the China Rock coordinate system such that $\theta = 0^\circ$ corresponds to normally incident waves and $+\theta$ corresponds to waves propagating in the $+y$

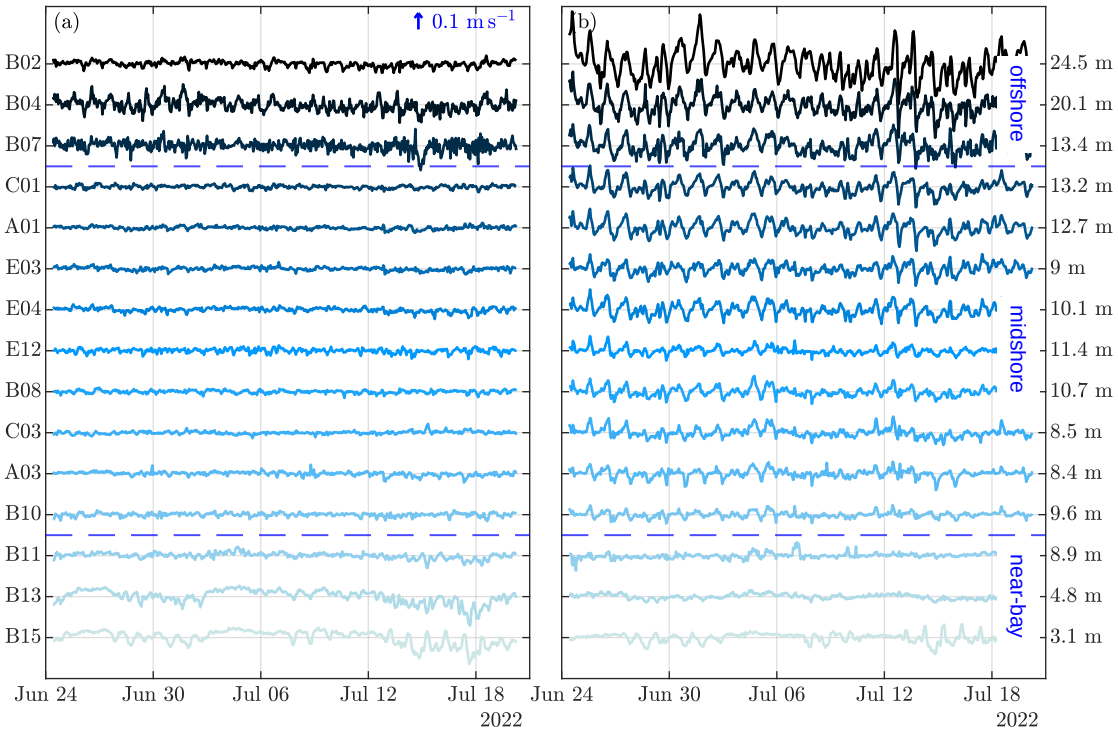

Figure 2.2. Time series of hourly depth-averaged (a) cross-shore u and (b) alongshore v currents. Times series are stacked and colormap set such that locations go from most offshore x coordinate (dark blue top) to most onshore x coordinate (light blue bottom). Location ID is on the left ordinate axis and mean bottom depth at that location is on the right ordinate axis. Scale of currents ± 0.1 m s^{-1} indicated by the blue bar in (a). *Offshore, midshore,* and *near-bay* regions indicated by the blue dashed lines and text in (b).

direction. Near-surface, an I-SPAR meteorological buoy was deployed at $(x, y) \approx (-900, 240)$m estimating wind stress just above the wave boundary layer at 5 m above the sea surface. Wind stress is estimated using the eddy covariance technique utilizing wind velocity and temperature measurements from an ultrasonic anemometer Chamberlain (2020). Wind stress measurements are hourly averaged with cross-shore τ_x and alongshore τ_y rotated into the China Rock coordinate system.

The hourly depth-averaged cross-shore u and alongshore v currents at each location are shown in figure 2.2. ADCP locations can be divided into three regions based on the currents behaviors and the bathymetric features at China Rock. The first region defined is the *offshore* region, which includes B02, B04, and B07 (figure 2.1). The currents (figure 2.2) are characterized

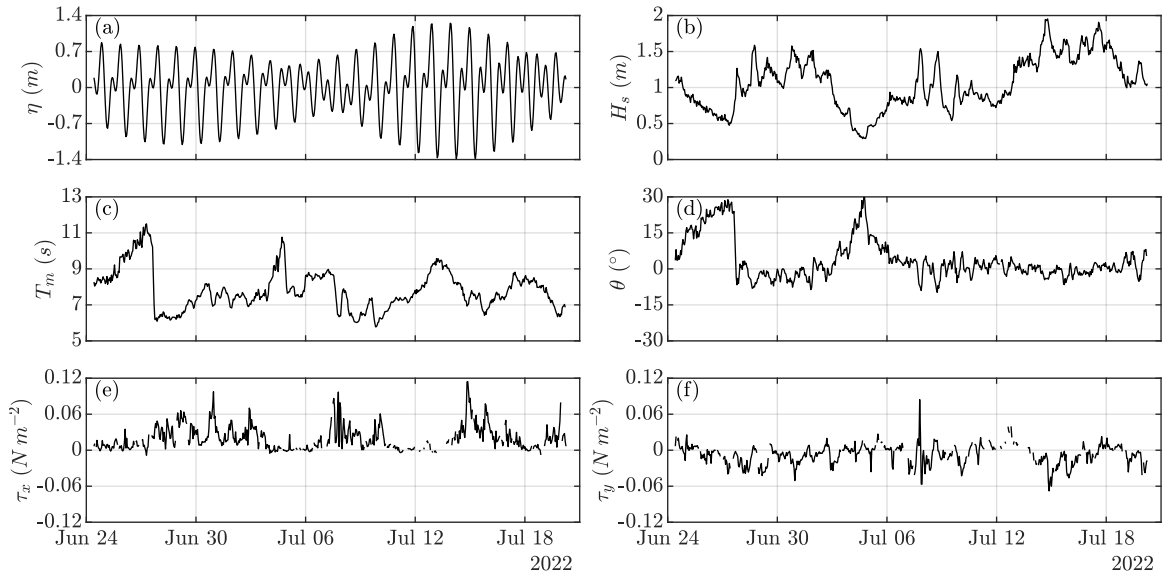

Figure 2.3. Time series of hourly means of potential forcings at location B08. (a) mean sea surface elevation (b) sea-swell band wave height H_s (c) sea-swell band mean period T_m (d) sea-swell band mean direction θ. Sea-swell band is from $0.06 Hz < f < 0.20$ Hz. At the location of the I-SPAR (e) cross-shore wind stress τ_x and (f) alongshore wind stress τ_y

by there relativly large *u* and *v* variability. The next region is the *midshore* region and includes the A line, C line, E line, B08 and B10 (figure 2.1). This region has the smallest *u* currents in the array and an onshore decrease in *v* current magnitude. The final region is the *near-bay* region and includes B11, B13, and B15 (figure 2.1). This region has increased *u* current magnitude and smaller *v* currents.

Timeseries of the principal expected circulation forcings spanning tide,waves, and wind at China Rock are shown in (figure 2.3). China Rock has a mixed semidiurnal tide typical of the central California coastline. During the experiment duration, a spring and neap tide cycle were observed. The maximum observed tidal range during the spring cycle was 2.63 m (figure 2.3a). Wave conditions were typical of summer during the experiment. The significant wave height was moderate with a mean of $H_s = 1.06$ m, minimum of $H_s = 0.29$ m, and a maximum of $H_s = 1.95$ m (figure 2.3b). Mean periods ranged from a minimum $T_m = 5.78$ s to a maximum $T_m = 11.50$ s, with an average $T_m = 7.83$ s (figure 2.3c). Mean direction was near normal incident $\theta = 0^\circ$ with an average direction of $\theta = 3.63^\circ$, minimum wave direction

was $\theta = -9.78^\circ$ while the maximum was larger at $\theta = 31.37^\circ$ (figure 2.3d). Wave statistics were dominated by subtidal variability. The magnitude of wind stress components was generally similar with a mean $\tau_x = 0.02\ \mathrm{N\,m^{-2}}$ and mean $\tau_y = -0.01\ \mathrm{N\,m^{-2}}$. Cross-shore wind stress τ_x (figure 2.3e)was primarily positive and thus blowing onshore, while the alongshore wind stress τ_y (figure 2.3f) was primarily negative. The majority of the variability in wind stress $|\tau| = \sqrt{\tau_x^2 + \tau_y^2}$ is predominantly subtidal.

Chapter 3

Results

3.1 Circulation

The variability of the depth-averaged currents is first examined using the rotary spectra S_w Gonella (1972) at three instrument locations (figure 3.1) selected from the B line to represent the offshore (B02), mid shore (B08) and the near-bay (B15) regions (figure 2.1). The rotary spectra S_w were computed from the complex velocity $w = u + iv$ using 144 hour Hanning windowed segments with 50% overlap yielding a frequency resolution of 0.0069 cph.

Across all frequency bands, S_w is generally largest at B02, decreases significantly at B08, then increases again at B15. In the subtidal band ($f < 1/33$ cph), S_w is red with the maximum at ± 0.0069 cph. In the diurnal ($1/33 < f < 1/16$ cph) and semidiurnal bands ($1/16 < f < 1/10$ cph) , distinct peaks in the rotary spectra occur at ± 0.0417 cph and ± 0.0833 cph corresponding to periods of approximately 24 h and 12 h. Due to the frequency resolution, distinct tidal constituents cannot be distinguished. Although not the focus of this analysis, harmonics of the diurnal and semidiurnal tide are evident at higher frequencies.

The maximum S_w in each frequency band is extracted at positive S_{w+} and negative S_{w-} peak frequency's. S_{w+}^{DU} peaks are larger than ST and SD peaks at all three locations (table 3.1). However, the size of the ST and SD peaks in comparison with the DU peaks varies at each location. The ratio S_{w+}^{ST}/S_{w+}^{DU} increases as locations get closer to shore at 0.23 at B02, 0.32 at B08, and 0.64 at B15. The ratio S_{w+}^{SD}/S_{w+}^{DU} is more constant throughout regions at 0.39 at B02,

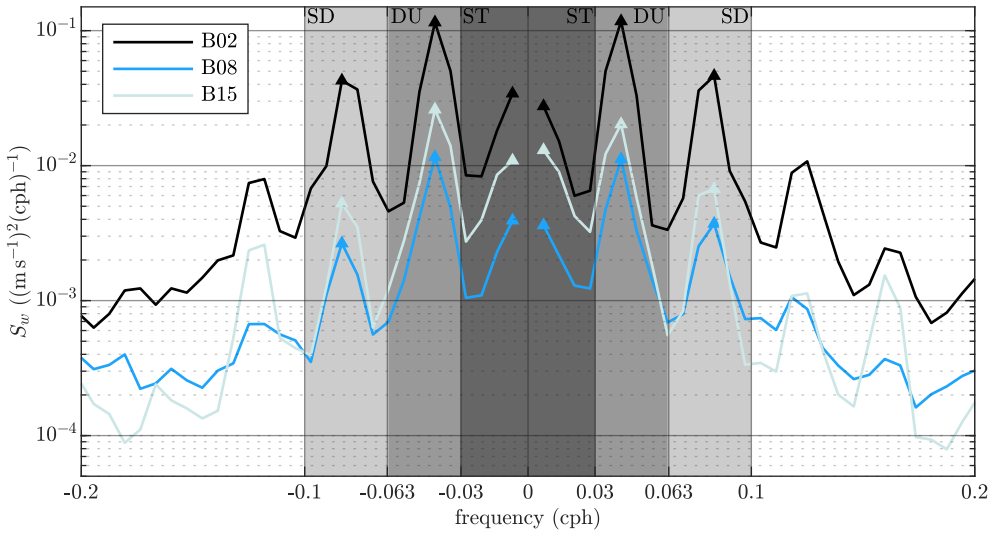

Figure 3.1. Depth-averaged current rotary spectra S_w versus frequency f at three locations (see figure 2.1): B02 (offshore), B08 (mid shore), and B15 (near-bay). The semidiurnal (SD, $1/16 < f < 1/10$ cph), diurnal (DU, $1/33 < f < 1/16$ cph), and subtidal (ST, $f < 1/33$ cph) frequency bands are indicated by grey shading. Positive and negative frequencies f are clockwise and counter- clockwise motions, respectively.

Table 3.1. Maximum S_w $[(\mathrm{m\,s^{-1}})^2\mathrm{cph^{-1}}]$ in each positive frequency band and ratio between positive and negative frequencies R for each frequency band.

ID	S_{w+}^{ST}	R^{ST}	S_{w+}^{DU}	R^{DU}	S_{w+}^{SD}	R^{SD}
B02	2.75×10^{-2}	0.90	11.74×10^{-2}	1.01	4.62×10^{-2}	1.04
B08	0.36×10^{-2}	0.96	1.12×10^{-2}	0.98	0.37×10^{-2}	1.18
B15	1.30×10^{-2}	1.09	2.03×10^{-2}	0.88	0.67×10^{-2}	1.13

0.33 at B08, and 0.33 at B15.

The ratio $R = \sqrt{S_{w+}/S_{w-}}$ between maxima S_w at positive S_{w+} and negative S_{w-} peak frequencies can be used to infer the type of motion at each location. If R is near 1, the motion is rectilinear, while if R is greater than or less than 1, the motion is rotational. At China Rock, the ratio $R \approx 1$ (table 3.1) for all locations and frequency bands implying that the motion is near rectilinear.

Using the same frequency bands from figure 3.1, subtidal $(u^{\mathrm{ST}}, v^{\mathrm{ST}})$, diurnal $(u^{\mathrm{DU}}, v^{\mathrm{DU}})$, and semidiurnal $(u^{\mathrm{SD}}, v^{\mathrm{SD}})$ hourly depth-averaged currents are estimated by consecutive low-pass filtering using the PL64 filter Limeburner (1985). The circulation is then further examined

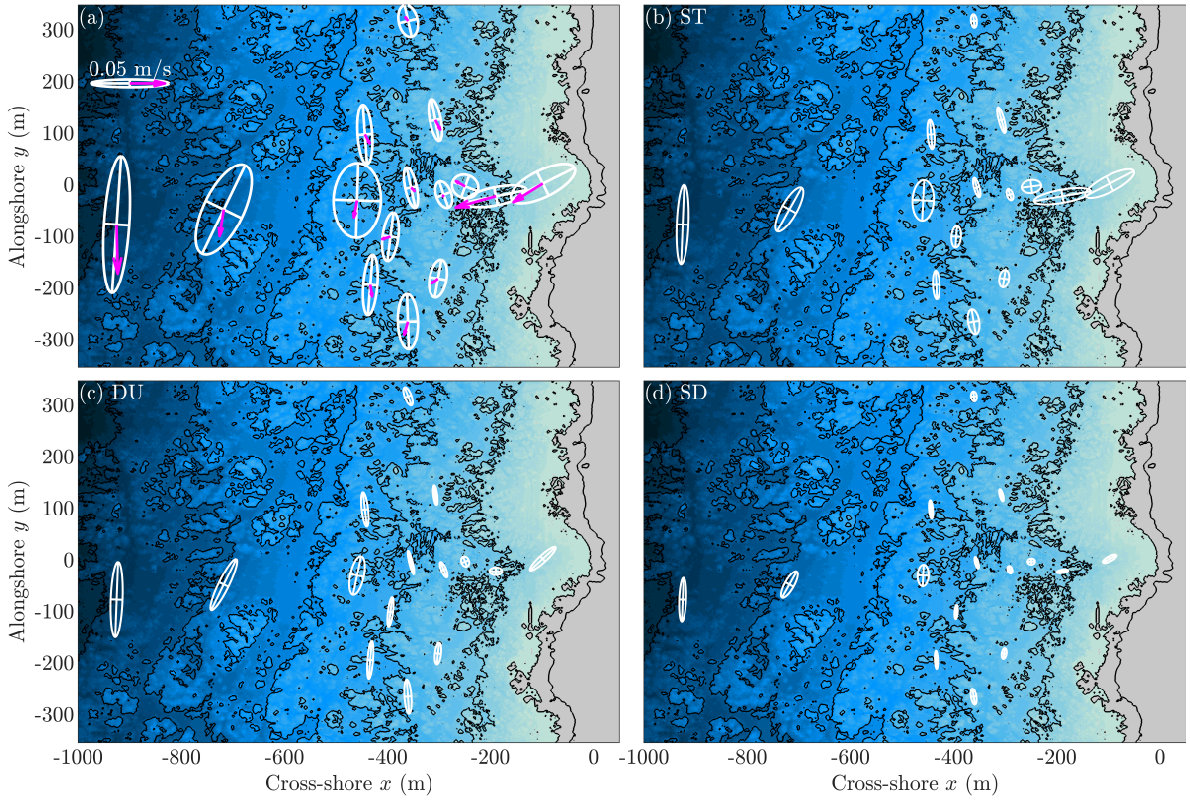

Figure 3.2. Mean (magenta arrows) and principal axes ellipses (white) of depth-averaged velocity in different frequency bands overlaid over the China Rock bathymetry in the local cross- and alongshore coordinate system: (a) unfiltered with mean arrows, (b) subtidal ST, (c) diurnal DU, (d) semidiurnal SD. Velocity scale of 0.05 $\mathrm{m\,s^{-1}}$ shown in (a).

by calculating mean currents and the principal component ellipses at each location. Variance ellipses were calculated for the unfiltered (u,v), sub tidal $(u^{\mathrm{ST}},v^{\mathrm{ST}})$, diurnal $(u^{\mathrm{DU}},v^{\mathrm{DU}})$ and semidiurnal $(u^{\mathrm{SD}},v^{\mathrm{SD}})$ current velocities (figure 3.2). Variance ellipses were derived for each band by calculating the major axis U_{maj}, minor axis U_{min}, and angle of the major axis θ_p. Current variability can be broadly categorized by U_{maj}, the aspect ratio $U_{\mathrm{maj}}/U_{\mathrm{min}}$, and θ_p. Aspect ratio $U_{\mathrm{maj}}/U_{\mathrm{min}}$ is defined such that larger values correspond to ellipses with more eccentricity and a minimum possible value of 1 corresponds to a circle. Principal angle θ_p is defined such that $|\theta_p| = 90^\circ$ is alongshore oriented and $|\theta_p| = 0^\circ$ is cross-shore oriented.

Deployment average cross-shore $\bar{u}$ and alongshore $\bar{v}$ flow (magenta arrows in figure 3.2a) is examined first. In both the offshore and midshore, $\bar{u}$ is small with $|\bar{u}| \lesssim 0.01$ $\mathrm{m\,s^{-1}}$. In the

near-bay, $\bar{u}$ is directed offshore and is strongest at B13 with $\bar{u} = -0.06\ \mathrm{m\,s^{-1}}$ and B15 with $\bar{u} = -0.04\ \mathrm{m\,s^{-1}}$. At the outer edge of the near-bay at B11, $\bar{u} = -0.01\ \mathrm{m\,s^{-1}}$ is much weaker. In the offshore region, $\bar{v}$ is directed towards in $-y$. At the outer edge of the offshore at B02, $\bar{v}$ is strongest at $\bar{v} = -0.07\ \mathrm{m\,s^{-1}}$. At the inner edge of the offshore region at B07, the $\bar{v}$ is weaker with $\bar{v} = -0.02\ \mathrm{m\,s^{-1}}$. In the midshore, $\bar{v}$ current is small with $|\bar{v}| \lesssim 0.02\ \mathrm{m\,s^{-1}}$ and also primarily directed towards $-y$. In the near-bay, alongshore currents are smallest at B11 $\bar{v} = 0.01\ \mathrm{m\,s^{-1}}$ and increase to $\bar{v} = -0.02\ \mathrm{m\,s^{-1}}$ at B13 and $\bar{v} = -0.03\ \mathrm{m\,s^{-1}}$at B15.

The unfiltered principal axes ellipses (figure 3.2a) are next examined from offshore to the near-bay. In the offshore, U_{maj} decreases as instruments get closer to shore from $U_{\mathrm{maj}} = 0.09\ \mathrm{m\,s^{-1}}$ at B02 to $U_{\mathrm{maj}} = 0.05\ \mathrm{m\,s^{-1}}$ at B07. A reduction in aspect ratio is also seen from $U_{\mathrm{maj}}/U_{\mathrm{min}} = 5.4$ at B02 to $U_{\mathrm{maj}}/U_{\mathrm{min}} = 1.6$ at B07. Principal angle in the offshore is alongshore and tilted along bathymetry with ranges from a minimum of $|\theta_p| = 64^\circ$ at B04 to a maximum of $|\theta_p| = 88^\circ$ at B07. In the midshore, U_{maj} is smaller and also decreases further onshore with ranges from $0.02 - 0.04\ \mathrm{m\,s^{-1}}$. In the alongshore on the E line, major axis decreases from $0.04\ \mathrm{m\,s^{-1}}$ E04 to $0.02\ \mathrm{m\,s^{-1}}$ at E12. Aspect ratio in the midshore decreases further onshore ranging from a maximum of $U_{\mathrm{maj}}/U_{\mathrm{min}} = 4.1$ at A01 to a minimum of $U_{\mathrm{maj}}/U_{\mathrm{min}} = 1.8$ at B10. Principal angle in the midshore is also alongshore and tilted along bathymetry with ranges from a minimum of $|\theta_p| = 70^\circ$ at B10 to a maximum of $|\theta_p| = 88^\circ$ at E04. In the near-bay, U_{maj} increases close to shore from minimum of $U_{\mathrm{maj}} = 0.02\ \mathrm{m\,s^{-1}}$ at B11 to a maximum of $U_{\mathrm{maj}} = 0.05\ \mathrm{m\,s^{-1}}$ at B15. Aspect ratio is near 1 at B11 with $U_{\mathrm{maj}}/U_{\mathrm{min}} = 1.2$ and increases to a maximum $U_{\mathrm{maj}}/U_{\mathrm{min}} = 3.5$ at B13. In the near-bay, principal angles were cross-shore oriented with a minimum value of $|\theta_p| = 11.3^\circ$ at B13 and maximum value of $|\theta_p| = 26.4^\circ$ at B15

The subtidal principal axes ellipses (figure 3.2b) are qualitatively very similar to the unfiltered with a few key differences. In the offshore and mid shore, $U^{\mathrm{ST}}_{\mathrm{maj}}$ is reduced to around 50% the size of U_{maj}, while in the near-bay is $U^{\mathrm{ST}}_{\mathrm{maj}}$ is still $70 - 90\%$ the size of U_{maj}. Subtidal aspect ratios $U^{\mathrm{ST}}_{\mathrm{maj}}/U^{\mathrm{ST}}_{\mathrm{min}}$ are were generally larger, but all were within $\pm 30\%$ of the unfiltered aspect ratios. Subtidal principal angles $|\theta^{\mathrm{ST}}_p|$ were generally very similar to the unfiltered, with

all locations within $\pm 15^\circ$ of $|\theta_p|$.

The diurnal ellipses (figure 3.2c) differ slightly more from the unfiltered and subtidal ellipses. In the offshore and midshore, $U_{\text{maj}}^{\text{DU}}$ are the largest of the filtered major axes at around 60% of the size of U_{maj}. However in the near-bay, $U_{\text{maj}}^{\text{DU}}$ decrease significantly at only $20-50\%$ the size of U_{maj}. $U_{\text{maj}}^{\text{DU}}/U_{\text{min}}^{\text{DU}}$ was larger than $U_{\text{maj}}/U_{\text{min}}$ at almost all locations. For example at B04 $U_{\text{maj}}^{\text{DU}}/U_{\text{min}}^{\text{DU}}$ was $2.2\times$ larger than the unfiltered. The only location in the diurnal band that did not see an increase relative to the unfiltered was B13 which had a $U_{\text{maj}}^{\text{DU}}/U_{\text{min}}^{\text{DU}}$ that was 50% smaller than that of the unfiltered. In the diurnal band, $|\theta_p^{\text{DU}}|$ is within 10° of unfiltered currents at all locations in the offshore and mid shore. However in the near-bay, $|\theta_p|$ becomes much more alongshore at most locations with $|\theta_p^{\text{DU}}| = 67.9^\circ$ at B11 and , $|\theta_p^{\text{DU}}| = 42.5^\circ$ at B15. The exception is B13 which becomes even more cross-shore at $|\theta_p^{\text{DU}}| = 0.6^\circ$.

The semidiurnal ellipses (figure 3.2d) are the last band examined. In the offshore and midshore $U_{\text{maj}}^{\text{SD}}$ is the smallest of the bands at around 30% of the size U_{maj}. In the near-bay, $U_{\text{maj}}^{\text{SD}}$ is reduced to only $20-30\%$ of the size of U_{maj}. Aspect ratio was $15\%-45\%$ larger in the offshore and at select location at the edge of the mid shore (A01,C01,E03.). However, The rest of the midshore and near-bay all saw $U_{\text{maj}}^{\text{SD}}/U_{\text{min}}^{\text{SD}}$ within $\pm 10\%$ of unfiltered at all sensors except B15 which saw an increase of 20%. Principal angles $|\theta_p^{\text{SD}}|$ were all within 15° of $|\theta_p|$.

3.2 Subtidal Forcing and Response

Here we analyze the forcing of the subtidal currents $(u^{\text{ST}}, v^{\text{ST}})$, which are split between two different regimes based on the circulation patterns (figure 3.2b). The first regime is wind driven and includes locations in the offshore and midshore where circulation was largely alongshore. The second regime is wave driven and includes locations in the near-bay, where circulation was largely cross-shore. We will examine these two regimes separately.

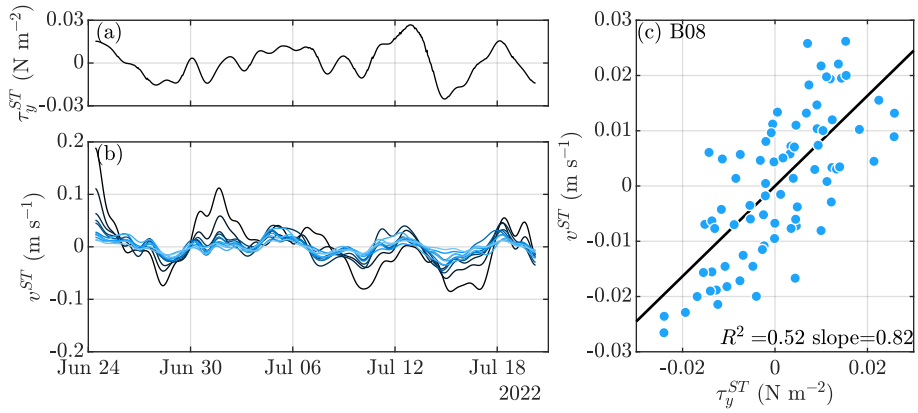

Figure 3.3. Times series of (a) subtidal alongshore wind stress τ_y^{ST} and (b) subtidal depth-averaged alongshore current v^{ST} across locations within the offshore and midshore. (c) Scatter plot of τ_y^{ST} versus v^{ST} in the center of the array at B08. Symbols represent sub sampling every 8 h. Black line is the least-squares best-fit slope related to the linear drag coefficient r_f by slope $= 1/(\rho_0 r_f)$. Squared correlation R^2 and best fit slope indicated in bottom right of (c).

3.2.1 Offshore and mid-shelf: Wind forcing

A clear visual relationship between the subtidal alongshore wind stress τ_y^{ST} (figure 3.3a) and the subtidal alongshore currents v^{ST} (figure 3.3b) is observed. For example, from 24–30 June a decrease in wind stress and currents coincide. The v^{ST} (figure 3.3b) decay in magnitude from offshore (darker) through the midshore (lighter blue), consistent with (figure 3.2b). We analyze the cross-shore decrease in v^{ST} within the context of enhanced bottom friction due to the rough bathymetry. We assume a simple balance between alongshore wind stress and linear bottom stress (e.g., Lentz and Winant, 1986), yielding the balance of

$$r_f v^{\mathrm{ST}} = \frac{\tau_y^{\mathrm{ST}}}{\rho}, \tag{3.1}$$

where r_f is a linear drag coefficient and $\rho = 1025\,\mathrm{kg\,m^{-3}}$. A linear least squares best fit of (3.1) is used to estimate r_f and fit skill R^2 at each location (figure 3.4). At B08, the LHS and RHS of (3.1) are clearly linearly related with fit-skill $R^2 = 0.52$ and $r_f = 1.2 \times 10^{-3}\ \mathrm{m\,s^{-1}}$ (figure 3.3c).

In the offshore region, R^2 steadily increases onshore from 0.15 at B02 to 0.55 at B07 (figure 3.4b). In the midshore region, R^2 ranged from a minimum of 0.30 at E12 to a maximum

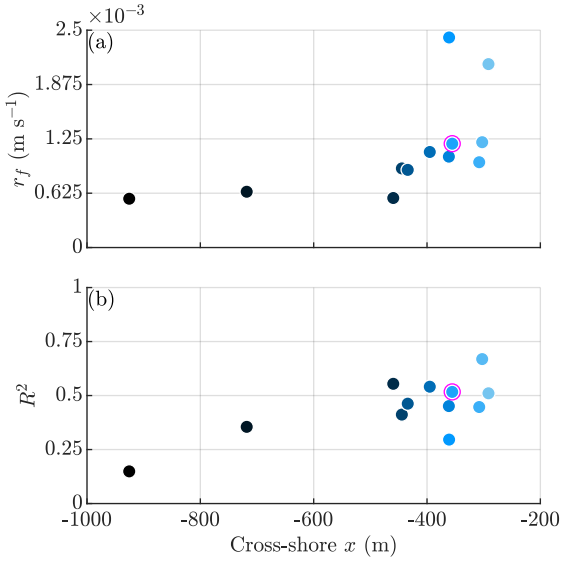

Figure 3.4. (a) Linear drag coefficient r_f and (b) fit-skill R^2 between τ_y^{ST} and v^{ST} versus cross-shore coordinate. Markers indicate locations in the offshore and midshore region. B08 indicated by magenta circle.

of 0.67 at A03. These R^2 values are consistent with previous balances (Lentz and Winant, 1986; Lentz et al., 1999; Liu and Weisberg, 2005; Kumar et al., 2015), and indicate that the subtidal alongshore dynamics are largely consistent with (3.1). In the offshore region, r_f (figure 3.4a) is effectively constant with a value of $\approx 6 \times 10^{-4}$ m s^{-1}. In the midshore region, r_f begins to rapidly increase to a value of 2.1×10^{-3} m s^{-1} onshore at B10. This onshore increase in r_f suggests increased bottom stress due to bed roughness. However, in the midshore, r_f also has significant spatial variability. For example, in the alongshore on the E-line (figure 2.1), $r_f = \{1.1, 1.0, 2.4\} \times 10^{-3}$ m s^{-1} at E03, E04, and E12, respectively. At E12, r_f is dramatically increased with corresponding low $R^2 = 0.3$ relative to other locations in similar depths and cross-shore location. This will be discussed in Section 4.2.

3.2.2 Near-bay: Wave forcing

Subtidal ellipses in the near-bay are all cross-shore oriented as opposed to alongshore oriented in the offshore and midshore (figure 3.2b), suggesting a different forcing mechanism. In Lentz et al. (2008), on a sandy and largely alongshore uniform inner-shelf, the Eulerian

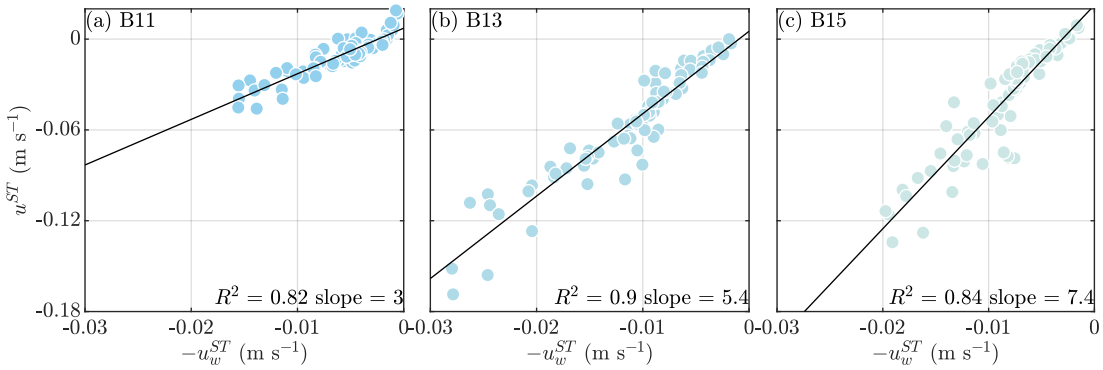

Figure 3.5. Subtidal depth-averaged cross-shore current u^{ST} versus subtidal depth-averaged Stokes drift velocity u_w^{ST} at (a) B11, (b) B13 and (c) B15. Symbols represent sub sampling every 8 h. Squared correlation R^2 and best fit slopes indicated in bottom right of each panel.

depth-averaged cross-shore flow largely balances the onshore wave-driven transport u_w on time scales much longer than subtidal. This wave-induced onshore flow u_w is,

$$u_w = \frac{Q_w}{h} \tag{3.2}$$

where Q_w is the onshore wave-induced Stokes transport Lentz et al. (2008),

$$Q_w \approx \frac{gH_s^2}{16c}\cos(\theta) \tag{3.3}$$

where, g is the gravitational acceleration, H_s the significant wave height, θ the wave direction relative to offshore ($\theta = 0^\circ$ for waves propagating directly onshore), and c is the wave speed. Wave speed c is estimated using linear theory assuming $c = \omega/k$ where $\omega = \sqrt{gk\tanh(kh)}$. H_s, θ, and h are all measured hourly at each location. Subsequently, u_w was subtidaly filtered yielding u_w^{ST}.

In the near-bay, u_w^{ST} and u^{ST} have a strong linear relation with $R^2 > 0.82$ at all 3 locations, suggesting that u^{ST} is likely wave driven. If the balance (3.2) held, the best-fit slope would be near-one. The best fit slope at each location is greater than one and the slope also increases onshore from 3 at B11 to 7.4 at B15, indicating greater Eulerian return flow than expected from

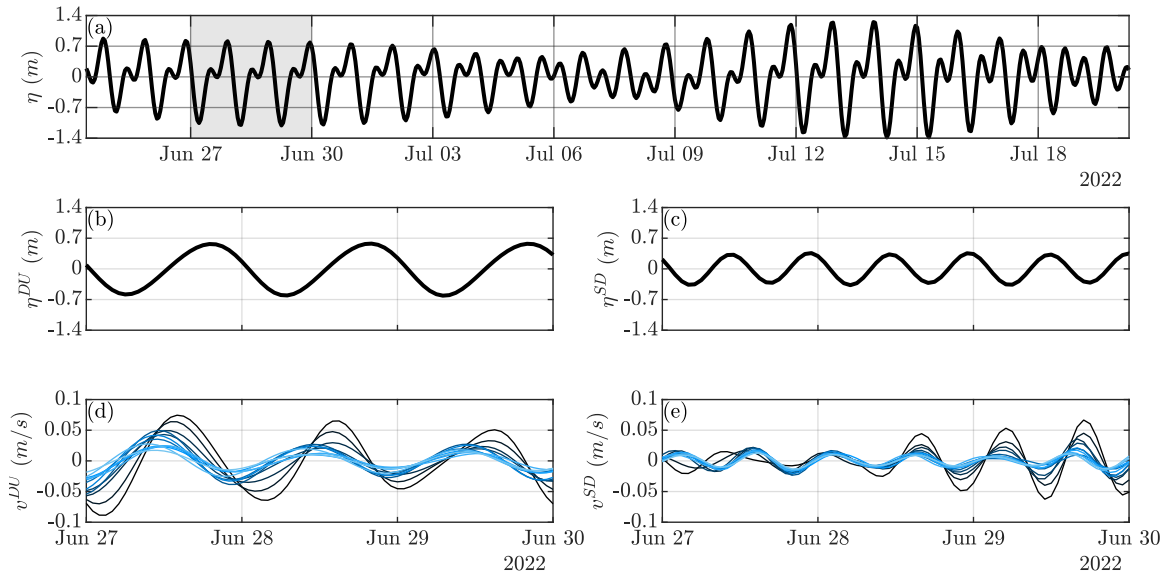

Figure 3.6. (a) Time series of hourly sea surface elevation η at B08. Three day time series (corresponding to grey shading) of (b) diurnal η^{DU} and (c) semidiurnal η^{SD} sea surface elevation (d) diurnal v^{DU} and (e) semidiurnal v^{SD} depth-averaged alongshore currents. Line colors in (d-e) corresponds locations with darker blue for more offshore and lighter blue for more onshore. Only offshore and midshore locations are shown.

that of an open coast inner-shelf (Lentz et al., 2008). The relationship $u^{\mathrm{ST}} = u_w^{ST}$ does not account for the geometry of the bay and thus the calculated u_w^{ST} underestimated the magnitude of the actual flow u^{ST} which will be examined in Section 4.3.

3.3 Tidal-band forcing and response

The analysis of the forcing of the tidal-band currents $(u^{\mathrm{DU}}, v^{\mathrm{DU}})$ and $(u^{\mathrm{SD}}, v^{\mathrm{SD}})$ will first focus on the offshore and midshore region. For both bands, DU and SD currents in the offshore and midshore are alongshore oriented and larger than in the near-bay. (figure 3.2c-d). The barotropic tide is expected to be the dominate forcing on tidal time scales. Other forcing (wind,waves) also contribute but their variability in the tidal bands is small in comparison to in the subtidal band where they dominated $\sigma_{H_s^{\mathrm{ST}}}/\sigma_{H_s} = 0.94$ and $\sigma_{\tau_y^{\mathrm{ST}}}/\sigma_{\tau_y} = 0.64$.

The sea surface elevation η is representative of the tide at China Rock (figure 3.6a). As China Rock has a mixed semidiurnal tide, η can be decomposed into diurnal η^{DU} (figure. 3.6b)

and semidiurnal η^{SD} (figure. 3.6c) components. The diurnal component has larger variability than the semidiurnal component with $\sigma_\eta^{DU}/\sigma_\eta = 0.68$ and $\sigma_\eta^{SD}/\sigma_\eta = 0.49$ respectively. The v^{DU} (figure 3.6d) is larger than v^{SD} (figure 3.6e) with σ_v^{DU}/σ_v ranging from 0.35 (B13) to 0.63 (A01) where σ_v^{SD}/σ_v ranged from 0.18 (B13) to 0.32 (E12). This larger σ_v^{DU}/σ_v than σ_v^{SD}/σ_v is consistent with the rotary spectra (figure 3.1) and principal axes ellipses (figure 3.2c-d). v^{DU} and v^{SD} both exhibit a decay in magnitude along with a phase shift from offshore to midshore resulting in midshore locations reaching their peak velocities before offshore locations.

At each location, estimates of the phase and magnitude-squared coherence between v and η as a function of frequency f are made. Magnitude-squared coherence C between v and η is defined as

$$C(f) = \frac{|P_{v\eta}(f)|^2}{P_{vv}(f)P_{\eta\eta}(f)}, \tag{3.4}$$

where $P_{vv}(f)$ and $P_{\eta\eta}(f)$ are auto-spectra and $P_{v\eta}(f)$ is the cross-spectra of the unfiltered timeseries. The phase $\Phi(f)$ is defined

$$\Phi(f) = \tan^{-1}\left[\frac{\mathrm{Im}\{P_{v\eta}(f)\}}{\mathrm{Re}\{P_{v\eta}(f)\}}\right], \tag{3.5}$$

in the interval $[-180^\circ, 180^\circ]$. Phase is defined such that negative (positive) Φ corresponds to peak v that occurs before (after) peak η. Magnitude-squared coherence $C(f)$ and phase $\Phi(f)$ are calculated using a Hamming window with a length of 129 samples and 64 samples of overlap. At the peak frequencies f_p for each band ($f_p^{\mathrm{DU}} = 0.0419$ cph, $f_p^{\mathrm{SD}} = 0.0805$ cph), $C(f_p)$ and $\Phi(f_p)$ are extracted for each location. The diurnal $T_p^{\mathrm{DU}} = 23.88$ is closet to the K1 (23.93 h) constituent while the semidiurnal $T_p^{\mathrm{DU}} = 12.42$ h is at the M2 (12.42 h) constitute.

We first examine the diurnal component v^{DU} of the alongshore currents. A consistent reduction in v^{DU} (figure 3.7a) is observed from $\sigma^{\mathrm{DU}} = 0.049\ \mathrm{m\,s^{-1}}$ offshore at B02 to onshore $\sigma^{\mathrm{DU}} = 0.010\ \mathrm{m\,s^{-1}}$ at B10 consistent with the three day time series in (figure 3.6d). The C^{DU} (figure 3.7c) is largely constant and ranges from a minimum of 0.64 (B07) to a maximum of

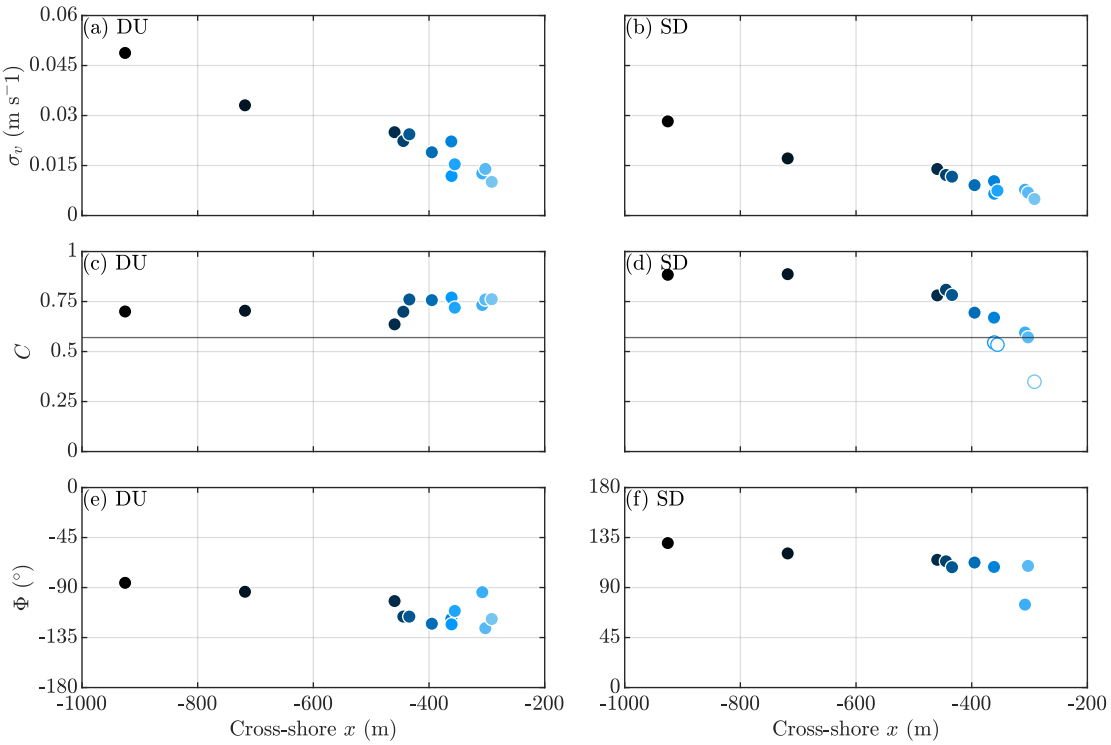

Figure 3.7. (left) Diurnal DU and (right) semidiurnal SD (a)-(b) standard deviation of alongshore velocity σ_V. (c)-(d) Magnitude-squared coherence C and (e)-(f) phase Φ at the peak frequencies between sea surface elevation η and alongshore velocity v versus cross-shore x. Only offshore and midshore location are shown. The 95% confidence interval on magnitude-squared coherence is $C \geq 0.57$ indicated by the line in (c)-(d). Locations that fall bellow this interval are unfilled in (d) and not shown in (f).

0.77 (E12) indicating a relation between v^{DU} and η^{DU}. The phase shifts Φ^{DU} (figure 3.7e) are negative and increase onshore with a minimum observed $\Phi^{\mathrm{DU}} = -86°$ (B02) and a maximum $\Phi^{\mathrm{DU}} = -126°$ (A03). This increase in negative phase shift with cross-shore coordinate is consistent with the three day time series in (figure 3.6d) where velocity peaks occurred before the tidal peak.

We next examine the semidiurnal component v^{SD} of the alongshore currents. A similar consistent reduction in v^{SD} (figure 3.7b) is observed from $\sigma^{\mathrm{SD}} = 0.028$ m s^{-1} offshore at B02 to onshore $\sigma^{\mathrm{DU}} = 0.005$ m s^{-1} at B10. σ^{SD} is approximately $0.5\times$ the size of σ^{DU} at all locations. The C^{SD} (figure 3.7d) is largest in the offshore regions and decrease from 0.88 (B02) to 0.78 (B07). In the midshore, C^{SD} continues to decrease onshore and is no longer above the 95%

confidence limit of $C \geq 0.57$ at B08, B10, and E12. The Φ^{SD} (figure 3.7f) is positive and decreases from offshore to the midshore from a maximum of $\Phi^{SD} = 130^{\circ}$ (B02) to a minimum of $\Phi^{SD} = 75^{\circ}$ (C03). This decrease in positive phase shift with cross-shore coordinate is consistent with the three day time series in (figure 3.6e) where velocity peaks occurred after the tidal peak.

Chapter 4

Discussion

Here we compare and contrast subtidal and tidal circulations statistics between the rocky shoreline of China Rock with the sandy alongshore-uniform inner- to mid-shelf of North Carolina and a coral reef on O'ahu to highlight circulation differences induced by the rocky shoreline.

4.1 Subtidal Circulation

We first compare the statistics of depth-averaged subtidal principal axes ellipses on the B-line at China Rock with a those of a representative sandy inner- to mid-shelf on the Outer Banks near Duck, North Carolina (Lentz et al., 1999). During the DUCK1994 experiment, a cross-shore line of moorings was deployed from August to early December 1994 at water depths of at 4-26 m, similar to those of the China Rock B-line spanning 3.1-24.5 m. However, the low-slope of the NC shelf results that the 26 m depth mooring was 16 km offshore in contrast to approximately 800 m offshore for the 24.5 m depth ADCP at China Rock (figure 2.1). Observed sandy-shelf currents from Duck were depth-averaged, hourly-averaged, and low-pass filtered with a similar cutoff period of 38 h (Lentz et al., 1999).

At the deeper locations with $h > 20$ m, the major axis of current variability $U^{\mathrm{ST}}_{\mathrm{maj}}$ (figure 4.1a) is 3–4$\times$ larger at Duck than at China Rock (figure 4.1). Some of this may be due to the larger alongshelf wind stress at Duck, ranging from $-0.5\ \mathrm{N\,m^{-2}}$ to $0.1\ \mathrm{N\,m^{-2}}$ whereas China Rock ranged from $-0.1\ \mathrm{N\,m^{-2}}$ to $0.2\ \mathrm{N\,m^{-2}}$. However, the cross-shore structure of $U^{\mathrm{ST}}_{\mathrm{maj}}$ at

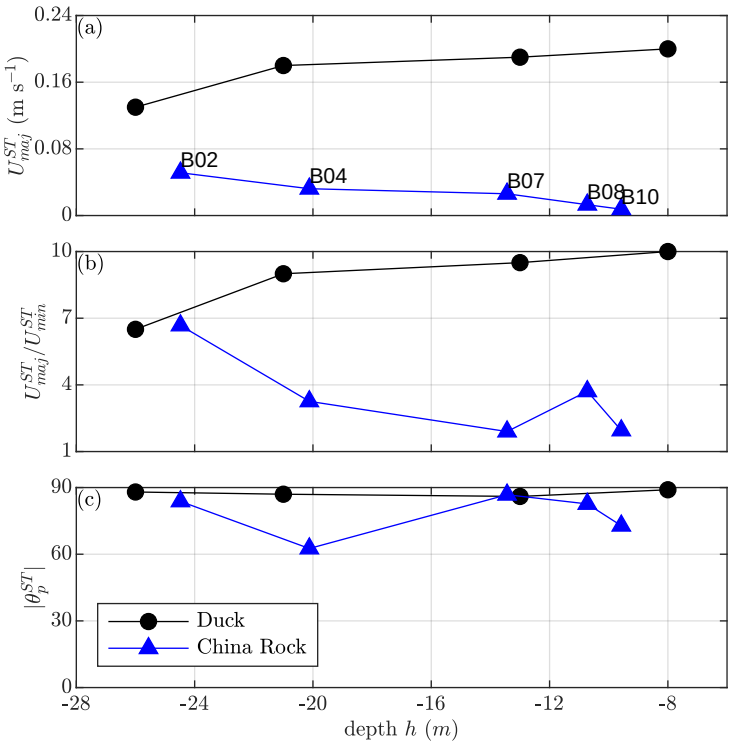

Figure 4.1. Subtidal principal axes ellipse parameters from Duck (black) and the B-line at China Rock (blue) versus water depth h: (a) Subtidal major axis $U^{\mathrm{ST}}_{\mathrm{maj}}$, (b) aspect ratio $U^{\mathrm{ST}}_{\mathrm{maj}}/U^{\mathrm{ST}}_{\mathrm{min}}$, and (c) principal angle $|\theta^{\mathrm{ST}}_p|$. Shown are offshore and midshore regions at China Rock and non-surfzone regions at Duck are shown. Duck observations from come from Table 1 of Lentz et al. (1999).

China Rock is very different from that of Duck. At China Rock, $U^{\mathrm{ST}}_{\mathrm{maj}} = 0.051\ \mathrm{m\,s^{-1}}$ is maximum offshore and decreases onshore to a minimum of $U^{\mathrm{ST}}_{\mathrm{maj}} = 0.001\ \mathrm{m\,s^{-1}}$ at $h = 9.6$ m. In contrast, at Duck $U^{\mathrm{ST}}_{\mathrm{maj}}$ increases into shallower water to a maximum of $U^{\mathrm{ST}}_{\mathrm{maj}} = 0.2\ \mathrm{m\,s^{-1}}$ at $h = 8$ m. This difference in $U^{\mathrm{ST}}_{\mathrm{maj}}$ cross-shore structure suggests that bottom stress is significantly enhanced in shallower water at China Rock relative to Duck.

The orientation of the subtidal principal axes ellipse $|\theta^{\mathrm{ST}}_p|$ is very different between China Rock and Duck (figure 4.1c). At Duck, $|\theta^{\mathrm{ST}}_p|$ is oriented almost perfectly alongshore from 26 to 4 m water depth with minimum of $|\theta^{\mathrm{ST}}_p| = 86°$. In contrast, in the China Rock offshore and midshore regions, $|\theta^{\mathrm{ST}}_p|$ deviated significantly from 90°, from $|\theta^{\mathrm{ST}}_p| = 84°$ at B02, with minima of $|\theta^{\mathrm{ST}}_p| = 63°$ at B04 and $|\theta^{\mathrm{ST}}_p| = 73°$ at B10. This variation in $|\theta^{\mathrm{ST}}_p|$ at China Rock can

likely be attributed to differences in large-scale bathymetric variability. Duck is approximately alongshore-uniform and smooth. In contrast, China Rock has alongshore bathymetric variability on scales of 100s of meters that likely impact and steer the subtidal flow at some ADCP locations. For example, at B04 the nearby 20 m depth contour is angled with respect to y-direction over approximately 200 m alongshore and large pinnacles are present just onshore and to the north and south (figure 2.1), which likely steered the flow off the alongshore direction leading to $|\theta_p^{\mathrm{ST}}| = 63^\circ$. Note that the DU and SD ellipses are similarly oriented at B04 and other locations (figure 3.2), consistent with bathymetric steering.

Offshore of $h > 22$ m depth, the aspect ratio of the subtidal principal axes ellipse $U_{\mathrm{maj}}^{\mathrm{ST}}/U_{\mathrm{min}}^{\mathrm{ST}}$ (figure 4.1b) are similar, 6.5 at Duck and 6.7 at China Rock, indicating similar flow polarization. Farther onshore, $U_{\mathrm{maj}}^{\mathrm{ST}}/U_{\mathrm{min}}^{\mathrm{ST}}$ increases to a maximum of 10 at $h = 8$ m for Duck and decreases to a minimum of 1.9 at $h = 9.6$ m for China Rock. Thus, the subtidal depth-averaged circulation is far more polarized at Duck than at China Rock. The onshore decrease of $U_{\mathrm{maj}}^{\mathrm{ST}}/U_{\mathrm{min}}^{\mathrm{ST}}$ at China Rock is likely due to the presence of bathymetric variability at 100+ m scales. This would not only steer the major axis of the subtidal flow, but also allow for less polarization as the subtidal depth-averaged flow veers with changing forcing.

4.2 Subtidal Linear Drag Coefficient

The estimated subtidal linear drag coefficient r_f (figure 3.4) across locations at China Rock is compared to previously reported r_f for sandy inner-shelves. The method of estimating of r_f here is similar to that used in previous where a balance between the depth-averaged alongshore current and alongshelf wind-stress balance in the subtidal band is assumed.

In Lentz and Winant (1986), an $r_f = 5 \times 10^{-4}$ m s^{-1} was estimated with $R^2 = 0.46$ at 15 m water depth within the Southern California Bight. On the North Carolina inner shelf, the estimated $r_f \approx \{2.7, 3.2, 3.6\} \times 10^{-4}$ m s^{-1} in water depths of 21 m, 13 m, and 8 m, respectively with $R^2 \approx 0.55$ (Lentz et al., 1999). On the San Pedro CA inner-shelf in 10 m water depth,

the estimated $r_f = 2.6 \times 10^{-4}$ m s^{-1} with $R^2 = 0.3$ (Kumar et al., 2015). At China Rock, the offshore (24–13 m water depth) region has $r_f \approx 6 \times 10^{-4}$, 2–3$\times$ larger than on the North Carolina inner-shelf, but only slightly larger than that in 15 m depth in the Southern California Bight. At China Rock, in water depths between 8–12 m, the r_f largely varies between 1–1.25 ($\times 10^{-3}$) with $R^2 \approx 0.5$. These values are 2.5–5$\times$ larger than those of the North Carolina and San Pedro CA inner-shelves. This further indicates that bottom stress is strongly enhanced in these water depths on a rocky inner-shelf.

We examine the larger China Rock linear drag coefficient relative to sandy inner-shelves by relating variations in r_f to the observed spatially-averaged bottom roughness $\bar{k}_{\mathrm{rms}}$. The China Rock bathymetry is detrended with a 20×20 m^2 plane yielding a perturbation depth $h'(x,y)$. The bed roughness $k_{\mathrm{rms}}(x,y)$ is estimated as the root-mean-square of h' over the 20×20 m^2 square. The spatially averaged $\bar{k}_{\mathrm{rms}}$ at each ADCP is then estimated by averaging $k_{\mathrm{rms}}(x,y)$ over a 50 m in x and 150 m in y rectangle centered at each location. The $\bar{k}_{\mathrm{rms}}$ at ADCP locations varied from 0.73–0.94 m. Results did not qualitatively change with different averaging rectangles. The linear bottom stress formulation,

$$\tau^b = \rho r_f v^{\mathrm{ST}}, \tag{4.1}$$

can be related to a quadratic stress formulation,

$$\tau^b = \rho C_D \langle |u_b| v_b \rangle, \tag{4.2}$$

where C_D is a non dimensional drag coefficient, (u_b,v_b) are near the seafloor but above the bottom boundary layer and $\langle\rangle$ represent a time-average over the sea-swell band. In wave dominated environments, a weak current and small wave angle approximation (e.g., Feddersen et al., 2000) leads to

$$\tau^b \approx \rho \tilde{C}_D U_{\mathrm{rms}} v^{\mathrm{ST}}, \tag{4.3}$$

where U_{rms} is the standard deviation of near-bed wave velocities, and $\tilde{C}_D$ includes an $O(1)$ factor

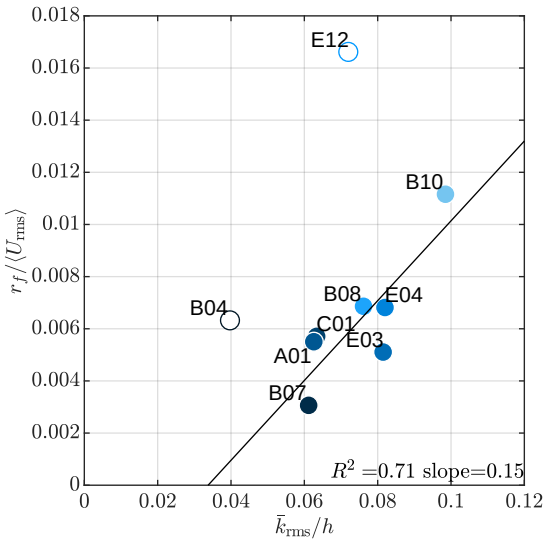

Figure 4.2. $r_f/\langle U_{\rm rms}\rangle$ versus $\bar{k}_{\rm rms}/h$ at ADCP locations. Location ID indicated by text and depth by color. Only locations in the offshore and midshore that had wave measurements required to estimate $\langle U_{\rm rms}\rangle$ are included. Outlier locations B04 and E12 are not filled. Squared correlation R^2 and best fit slopes between non-outlier locations (filled markers) indicated in bottom right.

accounting for averaging over the random waves. At ADCP locations that sampled pressure sufficiently rapidly, we use linear theory to estimate time series of $U_{\rm rms}$ in the sea-swell band (Marques et al., 2024). This is then averaged over the experiment duration to get a representative measure wave orbital velocity magnitude $\langle U_{\rm rms}\rangle$, which varied from 0.1–0.24 $\mathrm{m\,s^{-1}}$ across ADCP locations, generally much larger than $U^{\rm ST}_{\rm maj}$, indicating the weak current approximation is reasonable.

In geophysical boundary layers, C_D can be related to the bed roughness normalized by water depth $\bar{k}_{\rm rms}/h$ (e.g., Tennekes and Lumley, 1978; Lentz et al., 2016). As C_D is proportional to $r_f/\langle U_{\rm rms}\rangle$ in wave dominated environments (4.3), we examine the relationship between $r_f/\langle U_{\rm rms}\rangle$ and $\bar{k}_{\rm rms}/h$ (figure 4.2) to test the hypothesis that the enhanced bottom roughness is leading to increased bottom stress.

For most locations, a relationship between $\bar{k}_{\rm rms}/h$ and $r_f/\langle U_{\rm rms}\rangle$ is evident (figure 4.2), where increasing $\bar{k}_{\rm rms}/h$ leads to increased drag coefficient $r_f/\langle U_{\rm rms}\rangle$ with squared correlation of $R^2 = 0.71$. Two locations (B04 and E12) are outliers with $r_f/\langle U_{\rm rms}\rangle$ greater than the $\bar{k}_{\rm rms}/h$

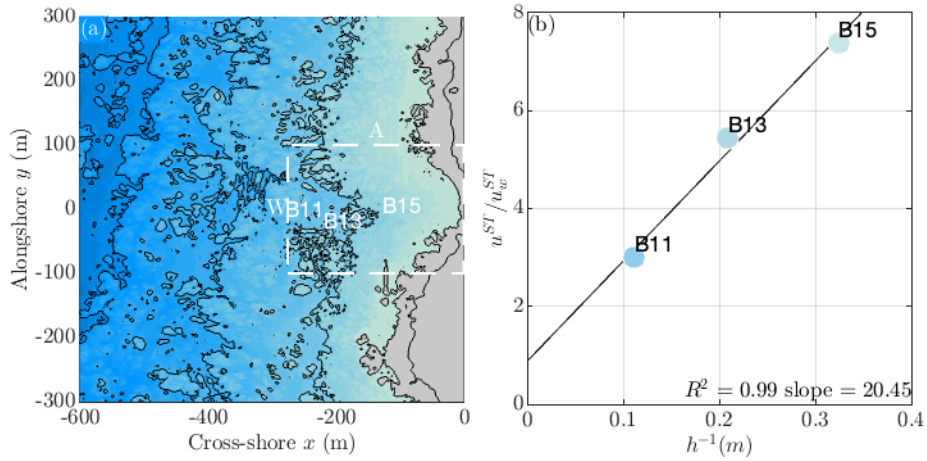

Figure 4.3. (a) Bathymetry at China Rock with white box showing the width W and cross-shore headland amplitude A of the bay. Instrument locations in the near-bay (B11,B13, and B15) denoted with white text. (b) Slope from figure 3.5 $u^{\mathrm{ST}}/u_w^{\mathrm{ST}}$ versus the inverse of bottom depth h^{-1} at locations in the near-bay. Squared correlation R^2 and best fit slope indicated in bottom right.

would suggest at the other locations (figure 4.2, unfilled circles). Both B04 and E12 are located near strong bathymetric variations at 100+ m scales (figure 2.1). As previously mentioned, at B04 the bathymetry contours are tilted with nearby large-scale pinnacles, leading to steering. Location E12 is located in a bathymetric canyon with shallower depths to the north and south, and is also an outlier in the midshore with $R^2 = 0.3$. A requirement to estimate r_f is that the alongshore momentum balance is a balance between wind stress and bottom stress. At these locations, likely other terms such as nonlinear advection may dominate. The overall linear relationship between $r_f/\langle U_{\mathrm{rms}}\rangle$ and $\bar{k}_{\mathrm{rms}}/h$ suggests that the enhanced bottom roughness elevates the bottom stress.

4.3 Wave-driven subtidal circulation in the near-bay

At a depth of $h = 5.2$ m on the sandy, alonshore-uniform shoreline of Duck NC with similar wave conditions ($\langle H_s\rangle = 0.9$ m, $\sigma_{H_s} = 0.5$ m), the observed depth-averaged subtidal offshore flow u^{ST} balanced expected onshore Stokes-drift flow u_w^{ST} with very high skill $R^2 = 0.94$ and a best-fit slope of ≈ 1 (Lentz et al., 2008). This is in contrast to in the near-bay at China

Rock ($h = 8.9, 4.8, 3.1$ m) and ($\langle H_s \rangle = 1.1$ m, $\sigma_{H_s} = 0.4$ m), where the the skill was also high $R^2 = 0.82$-0.90 but the best-fits slopes were much larger ranging from 3-7.4 (figure 3.5), indicating the offshore velocity in the center of the bay is greater than implied by Stokes-drift. The increased best-fit slopes suggest that another, unaccounted for factor increases u relative to u_w, likely bathymetric effects from the embayment. These bathymetric effects seem to depend on depth, as $u^{\mathrm{ST}}/u_w^{\mathrm{ST}}$ increases as locations get shallower at each location in the bay (figure 4.3b). Circulation in embayments can be diagnosed using a parameter R_{bay} (Conlin et al., 2024),

$$R_{\mathrm{bay}} = \frac{kh}{A/W}, \tag{4.4}$$

representing a ratio between wave refraction and bay geometry effects. The bay's geometry is quantified by it's alongshore width W and cross-shore headland amplitude A (figure 4.3a), and depth h is taken near the alongshore-center and offshore edge of the bay. Wave conditions are accounted for using the wave number k which is calculated using linear wave theory. For very large values of R_{bay}, circulation is expected to resemble that of a more alongshore uniform shoreline. Smaller kh (more refraction) or larger A/W lead to smaller R_{bay}, for which different circulation can be expected due headland wave focusing. At China Rock, we estimate the bay width $W = 200$ m as the alongshore distance between the most offshore location of the $z = 0$ m contour on both sides of the bay (figure 4.3a). The headland amplitude A is estimated as the distance from the most onshore location of the $z = 0$ m contour to most offshore extent off the $z = 5$ m contour where the shape of the bay can still be seen. At China Rock, an $R_{bay} = 0.63$ was observed using deployment average k estimated at B11, a depth $h = 9$ m, width $W = 200$ m, and amplitude $A = 275$ m. This is very similar to a nearby rocky shoreline Asilomar (Conlin et al., 2024), which featured a $R_{bay} = 0.6$ using a depth $h = 4$ m, width $W = 200$ m, and amplitude $A = 150$ m. Surface circulation in this embayment was dominated by a rip current at the center of the embayment with alongshore feeder currents emanating from both headlands forced by wave focusing and breaking on the headlands. Based on the values of R_{bay}, it's very likely that

similar processes are occurring at China Rock resulting in the larger u in the bay.

4.4 Tidal velocity attenuation and phase shift

We now compare the alongshore tidal currents on three different types of shorelines. On the sandy inner-shelf of Duck NC at depths $h = 8$-26 m, tidal current principal axes ellipses and phase shifts for semidiurnal (M2) and diurnal (combined K1/P1) tide constituents were estimated (Lentz et al. (2001) table 1. and table 2a-b.). On a fringing coral reef shelf on the western coast of O'ahu, Hawai'i, attenuation V/V_0 and phase shift $\Delta\Phi$ of alongshore depth-averaged currents in relation to the semidiurnal tide is examined at depths $h = 6$-24 m (Amador et al. (2020) figure 9.). We compare these observations on both sand and coral reefs to the portion of the B line that spans similar depths from B10 ($h = 9.6$ m) to B02 ($h = 24.5$ m). While depths are similar across all three shorelines, the cross-shore width at Duck is significantly wider at ≈ 20 km when compared to the narrower widths of ≈ 600 m on O'ahu and at China Rock.

In Amador et al. (2020), attenuation $V/V_0 = \sqrt{C_1^2 + C_2^2}$ and phase shift $\Delta\Phi = \tan^{-1} C_1/C_2$ are estimated from the linear least squares fit of a sinusoidal function $v = C_1 \sin\Phi + C_2 \cos\Phi$ to the depth-averaged alongshore current. We will define a similar attenuation V/V_0 at each location at China Rock and Duck as the ratio $U_{\text{maj}}/|U_{\text{maj}}|$ where U_{maj} is taken at each instrument location and $|U_{\text{maj}}|$ is the maximum observed velocity in the direction of the major axis for each shoreline.

In the diurnal band at China Rock, an onshore decrease is observed from $V/V_0 = 1$ at B02 ($h = 24.5$ m) to $V/V_0 = 0.2$ at B10 ($h = 9.6$ m). This is in contrast to Duck an onshore increase is observed from $V/V_0 = 0.5$ at $h = 26$ m to $V/V_0 = 1$ at $h = 8$ m. Phase shifts were slightly larger across the same depths at 32° for China Rock versus 23° at Duck.

In the semidiurnal band, an onshore decrease in V/V_0 is observed at all three shorelines. At Duck and on O'ahu, $V/V_0 = 0.5$ at depths of $h = 8$ m and $h = 6$ m respectively. China Rock once again has a larger decrease with $V/V_0 = 0.2$ at $h = 9.6$ m. Phase differences are compared

across a smaller range of depths as phase estimates at B08 and B10 at China Rock did not have corresponding magnitude-squared coherence that was significant at the 95% confidence level. At China Rock (B02-B07,$h = 24.6$-13.4 m) and at Duck ($h = 26$-14 m) very similar phase differences of 15° and 14° are observed. On O'ahu ($h = 24$-14 m), a larger phase difference of 30° is observed.

In both the diurnal and semidiurnal bands, China Rock has a larger attenuation of alongshore tidal velocity when compared to a sandy shore (Duck) or coral reef (O'ahu). This larger attenuation can likely be attributed to enhanced bottom roughness. At scales from 4 m to 20 m at China Rock, our estimated $k_{\mathrm{rms}} \approx 0.75$ m. In contrast, at scales from 4–16 m on O'ahu, the Amador et al. (2020) bed roughness was ≈ 0.1 m. Phase differences between currents does not seem to be affected by bottom roughness with the largest shifts being seen on O'ahu while the shifts at Duck and China Rock were generally very similar.

Chapter 5

Summary

The variability in the depth-average circulation at China Rock primarily occurred on subtidal, diurnal, and semidiurnal time scales. Between the three regions defined (offshore,midshore, and near-bay), the offshore and midshore regions were found to have distinct circulation differences from the near-bay region.

In the offshore and midshore, circulation was primarily driven by along shelf wind stress on subtidal time scales and the barotropic tide on tidal time scales. Across all three frequency bands, principal-axes ellipses were oriented alongshore/along bathymetry with an onshore decay in U_{maj} size due to the effects of strong bottom friction. Diurnal $U_{\mathrm{maj}}^{\mathrm{DU}}$ was largest followed by subtidal $U_{\mathrm{maj}}^{\mathrm{ST}}$and semidiurnal $U_{\mathrm{maj}}^{\mathrm{SD}}$.

Bottom friction in this region was estimated using a linear drag coefficient r_f estimated from a balance between depth-averaged alongshore subtidal currents v^{ST} and wind stress τ_y^{ST}. The values of r_f at China Rock increased onshore and were found to be larger than those values estimated for sandy inner shelves. Ratios between linear drag and near-bed wave velocities $r_f/\langle U_{\mathrm{rms}}\rangle$ were found to be related to the ratios of spatially averaged roughness and depth $\bar{k}_{\mathrm{rms}}/h$ at each location. At most locations, higher drag coefficients r_f were seen at locations with reduced depth h and/or increased spatially averaged roughness $\bar{k}_{\mathrm{rms}}$.

Due to the increased bottom friction, subtidal circulation at China Rock was found to differ from a representative sandy shoreline of Duck, NC for similar depths (h = 8-26 m).

Principal axes ellipses at China Rock featured smaller major axes $U^{\mathrm{ST}}_{\mathrm{maj}}$ that decay onshore which is in contrast to Duck which featured larger $U^{\mathrm{ST}}_{\mathrm{maj}}$ that strengthened onshore. Aspect ratio $U^{\mathrm{ST}}_{\mathrm{maj}}/U^{\mathrm{ST}}_{\mathrm{min}}$ was also smaller at China Rock and decayed onshore compared to Duck which saw larger $U^{\mathrm{ST}}_{\mathrm{maj}}/U^{\mathrm{ST}}_{\mathrm{min}}$ that increased onshore. Principal angle $|\theta_p|$ was alongshore oriented on both shorelines, however China Rock saw significantly more variability in $|\theta_p|$ than Duck.

Tidal circulation is also affected by bottom roughness with attenuation of alongshore tidal currents being greater than what has been observed on a representative sandy shoreline and coral reef. Phase differences between alongshore currents do not seem to be affected by bottom roughness with the largest shifts occurring on a coral reef while the shifts on a sandy shoreline and rocky shoreline were generally very similar.

In the near-bay region, principal axes ellipses were cross-shore oriented and U_{maj} was largest in the subtidal band with much smaller values in the diurnal and semidiurnal bands. Cross-shore currents in this region were driven by Strokes drift from surface gravity waves consistent with what was observed at Duck for similar depths. However, cross-shore currents at China Rock were larger than Stokes drift would suggest. The geometry and wave conditions off the bay at China Rock are are comparable with Asilomar, a nearby rocky bay.

Bibliography

Amador, A., I. B. Arzeno, S. N. Giddings, M. A. Merrifield, and G. Pawlak, 2020: Cross-shore structure of tidally driven alongshore flow over rough bathymetry. *Journal of Geophysical Research: Oceans*, **125 (8)**, https://doi.org/https://doi.org/10.1029/2020JC016264.

Arzeno, I. B., A. Collignon, M. Merrifield, S. N. Giddings, and G. Pawlak, 2018: An alongshore momentum budget over a fringing tropical fore-reef. *Journal of Geophysical Research: Oceans*, **123 (11)**, 7839–7855, https://doi.org/https://doi.org/10.1029/2018JC014238.

Austin, J. A., and S. J. Lentz, 2002: The inner shelf response to wind-driven upwelling and downwelling. *Journal of Physical Oceanography*, **32**, 2171–2193.

Bird, E., 2008: *Coastal geomorphology: An introduction, 2nd edition*. John Wiley and Sons.

Castelle, B., and G. Coco, 2013: Surf zone flushing on embayed beaches. *Geophysical Research Letters*, **40 (10)**, 2206–2210, https://doi.org/https://doi.org/10.1002/grl.50485.

Chamberlain, V. D., 2020: I-spar buoy: Design of a lightweight shallow water air-sea measurement platform. *Naval Postgraduate School*.

Conlin, M. P., G. Wilson, J. H. MacMahan, and O. B. Marques, 2024: Rip current surface circulation in a small rocky shore embayment. *Journal of Geophysical Research: Oceans*, submitted.

Feddersen, F., R. T. Guza, S. Elgar, and T. H. C. Herbers, 2000: Velocity moments in alongshore bottom stress parameterizations. *Journal of Geophysical Research: Oceans*, **105 (C4)**, 8673–8686, https://doi.org/10.1029/2000JC900022.

Fewings, M. R., and S. J. Lentz, 2010: Momentum balances on the inner continental shelf at Martha's Vineyard Coastal Observatory. *J. Geophysical Res. Oceans*, **115**, https://doi.org/{10.1029/2009JC005578}.

Fewings, M. R., and S. J. Lentz, 2011: Summertime cooling of the shallow continental shelf. *J. Geophysical Res. Oceans*, **116 (C7)**, https://doi.org/10.1029/2010JC006744.

Gonella, J., 1972: A rotary-component method for analysing meteorological and oceanographic vector time series. *Deep Sea Research and Oceanographic Abstracts*, **19 (12)**, 833–846, https://doi.org/{10.1016/0011-7471(72)90002-2}.

Hench, J. L., J. J. Leichter, and S. G. Monismith, 2008: Episodic circulation and exchange in a wave-driven coral reef and lagoon system. *Limnology and Oceanography*, **53 (6)**, 2681–2694, https://doi.org/https://doi.org/10.4319/lo.2008.53.6.2681.

Johnson, M. E., 1988.: Why are ancient rocky shores so uncommon? *Geology*, **96**, 469–480.

Kirincich, A. R., S. J. Lentz, and J. A. Barth, 2009: Wave-driven inner-shelf motions on the oregon coast. *J. Phys. Oceanogr.*, **39**, 2942–2956, https://doi.org/10.1175/2009JPO4041.1.

Kumar, N., F. Feddersen, Y. Uchiyama, J. McWilliams, and W. O'Reilly, 2015: Midshelf to surfzone coupled ROMS-SWAN model data comparison of waves, currents, and temperature: Diagnosis of subtidal forcings and response. *J. Physical Oceanography*, https://doi.org/10.1175/JPO-D-14-0151.1.

Lentz, S., M. Carr, and T. H. C. Herbers, 2001: Barotropic tides on the north carolina shelf. *Journal of Physical Oceanography*, **31 (7)**, 1843 – 1859, https://doi.org/10.1175/1520-0485(2001)031⟨1843:BTOTNC⟩2.0.CO;2.

Lentz, S., R. T. Guza, S. Elgar, F. Feddersen, and T. H. C. Herbers, 1999: Momentum balances on the North Carolina inner shelf. *J. Geophysical Res.*, **104**, 18 205–18 240, https://doi.org/10.1029/1999JC900101.

Lentz, S. J., 1994: Current dynamics over the northern california inner shelf. *J. Phys. Oceanogr.*, **24**, 2461–2478, https://doi.org/10.1175/1520-0485(1994)024⟨2461:CDOTNC⟩2.0.CO;2.

Lentz, S. J., J. H. Churchill, K. A. Davis, J. T. Farrar, J. Pineda, and V. Starczak, 2016: The characteristics and dynamics of wave-driven flow across a platform coral reef in the red sea. *Journal of Geophysical Research: Oceans*, **121 (2)**, 1360–1376, https://doi.org/https://doi.org/10.1002/2015JC011141.

Lentz, S. J., M. Fewings, P. Howd, J. Fredericks, and K. Hathaway, 2008: Observations and a model of undertow over the inner continental shelf. *J. Physical Oceanography*, **38 (11)**, 2341–2357, https://doi.org/{10.1175/2008JPO3986.1}.

Lentz, S. J., and M. R. Fewings, 2012: The wind- and wave-driven inner-shelf circulation. *Annual Review of Marine Science*, **4 (1)**, 317–343, https://doi.org/10.1146/annurev-marine-120709-142745.

Lentz, S. J., and C. D. Winant, 1986: Subinertial currents on the Southern California shelf. *J. Phys. Oceanogr.*, **16**, 1737–1750, https://doi.org/10.1175/1520-0485(1986)016⟨1737:SCOTSC⟩2.0.

CO;2.

Limber, P. W., and A. B. Murray, 2014: Unraveling the dynamics that scale cross-shore headland relief on rocky coastlines: 2. model predictions and initial tests. *Journal of Geophysical Research: Earth Surface,*, **119(4)**, 874–891.

Limber, P. W., A. B. Murray, P. N. Adams, and E. B. Goldstein, 2014: Unraveling the dynamics that scale cross-shore headland relief on rocky coastlines: 1. model development. *Journal of Geophysical Research: Earth Surface*, **119(4)**.

Limeburner, C., R., 1985: Code-2: Moored array and large-scale data report. *WHOI Tech. Rep. 85-35/CODE Tech. Rep. 38, 234 pp*.

Liu, Y., and R. H. Weisberg, 2005: Momentum balance diagnoses for the west florida shelf. *Continental Shelf Research*, **25 (17)**, 2054–2074, https://doi.org/https://doi.org/10.1016/j.csr.2005.03.004.

Luijendijk, A., G. Hagenaars, R. Ranasinghe, F. Baart, G. Donchyts, and S. Aarninkhof, 2018: The state of the world's beaches. *Scientific reports*, **8(1)**, 6641.

MacMahan, J., E. Thornton, S. Dressel, and M. Cook, 2024: Intermediate wave scale rocky bottom variability for the nearshore along california. *Journal of Geophysical Research: Earth Surface*, submitted.

MacMahan, J., E. Thornton, N. Patria, C. Gon, and M. Denny, 2023: Rip currents off rocky-shore surge channels. *Journal of Geophysical Research: Oceans*, **128 (8)**, https://doi.org/https://doi.org/10.1029/2022JC019317, URL https://agupubs.onlinelibrary.wiley.com/doi/abs/10.1029/2022JC019317.

Marques, O. B., F. Feddersen, and J. H. MacMahan, 2024: Wave energy dissipation by bottom friction on rocky shores. *Journal of Physical Oceanography*, submitted.

Mitchum, G. T., and A. J. Clarke, 1986: The frictional nearshore response to forcing by synoptic scale winds. *J. Phys. Oceanogr.*, **16**, 934–946, https://doi.org/10.1175/1520-0485(1986)016⟨0934:TFNRTF⟩2.0.CO;2.

Monismith, S. G., 2007: Hydrodynamics of coral reefs. *Annual Review of Fluid Mechanics*, **39 (Volume 39, 2007)**, 37–55, https://doi.org/https://doi.org/10.1146/annurev.fluid.38.050304.092125.

Morgan, S. G., A. L. Shanks, J. H. MacMahan, A. J. Reniers, and F. Feddersen, 2018: Planktonic subsidies to surf-zone and intertidal communities. *Annual Review of Marine Science*, **10**, 345–369, https://doi.org/10.1146/annurev-marine-010816-060514.

Moulton, M., S. H. Suanda, J. C. Garwood, N. Kumar, M. R. Fewings, and J. M. Pringle, 2023: Exchange of plankton, pollutants, and particles across the nearshore region. *Annual Review of Marine Science*, **15**, 167–202, https://doi.org/10.1146/annurev-marine-032122-115057.

Sinnett, G., and F. Feddersen, 2019: The nearshore heat budget: Effects of stratification and surfzone dynamics. *Journal of Geophysical Research: Oceans*, **124 (11)**, 8219–8240, https://doi.org/10.1029/2019JC015494.

Tennekes, H., and J. Lumley, 1978: *A FIRST COURSE IN TURBULENCE*. MIT PRESS, URL https://books.google.com/books?id=W_8EvwEACAAJ.

Trowbridge, J. H., and S. J. Lentz, 2018: The bottom boundary layer. *Annual Review of Marine Science*, **10 (Volume 10, 2018)**, 397–420, https://doi.org/https://doi.org/10.1146/annurev-marine-121916-063351.

Weisberg, R. H., Z. Li, and F. Muller-Karger, 2001: West florida shelf response to local wind forcing: April 1998. *J. Geophys. Res.*, **106**, 31 239–31 262, https://doi.org/10.1029/2000JC000529.